Optimization of array configurations and panel combinations for the detection and imaging of abandoned mineshafts using 3D cross-hole electrical resistivity tomography.

Paul B. Wilkinson[1], Jonathan E. Chambers[1], Philip I. Meldrum[1], Richard D. Ogilvy[1] and Simon Caunt[2].

[1] British Geological Survey, Kingsley Dunham Centre, Keyworth, Nottingham, NG12 5GG, UK

[2] The Coal Authority, 200 Lichfield Lane, Mansfield, NG18 4RG, UK

Abstract

Cross-borehole electrical resistivity tomography was used to detect and image a concealed air-filled mineshaft at a greenfield test site. The measurement configurations and panel combinations were selected using a two-stage optimization process. An optimal set of array configurations was selected for each cross-borehole panel on the basis of the model resolution matrix. Subsequently, various combinations of panels were tested with synthetic and field data to determine the effects of coverage and data density on the resulting tomographic image. In the field trials, complicating factors were introduced by the use of resistive cement linings in the boreholes. A resistive feature was detected between the boreholes using a single panel and a 2.5D inversion, but the image quality was too poor to identify this as a mineshaft. A much-improved image was obtained using eight boreholes and eight panels with a full 3D inversion. Only four of these panels intersected the shaft. Crucially, the other panels provided coverage of outlying regions of the model, enabling the inversion algorithm to distinguish between the resistive effects of the borehole linings and the mineshaft.

Introduction

The UK has a considerable legacy of mining stretching back over hundreds of years that affects both the urban and rural environments. Hidden and abandoned mine entries and shafts can pose serious risks to health and safety and can, according to some, influence property values in affected areas. Consequently, the identification of reliable geophysical techniques for detecting and imaging concealed mine entries is highly desirable for assessing the associated risks and liabilities with greater confidence. The work presented here was carried out for the Coal Authority as a part of a wider investigation into this problem. It can be difficult or impossible to undertake surface tomographic surveys in the built environment. However cross-borehole tomography would seem to be an ideal technique to determine whether a particular region, for example directly beneath a building, contained hidden void spaces. There are various geophysical methods that can be employed in a cross-hole configuration, but only seismic tomography has been extensively used and demonstrated in this context (Nath, 2004; Orlowsky *et al*., 2003; Misiek *et al*., 2001; Rechtien *et al*., 1995). We were able to find just one study that describes the use of cross-hole electrical resistivity tomography (ERT) to detect uncharted mines (Maillol *et al*., 1999). In that report, 2.5D algorithms were used to invert field and synthetic ERT data from pairs of boreholes (panels). That study found that cross-hole ERT was effective in detecting conductive water-filled voids, but was not able to detect resistive air-filled cavities.

In this paper, we examine the optimization of measurement configurations and panel combinations to enable the detection and imaging of an air-filled mineshaft at a known location in a greenfield test site. Eight boreholes were used, equally spaced around a 15 m diameter circle centered on the shaft. Data from single and multiple panels were inverted using 2.5D and 3D algorithms respectively to produce tomographic images of the subsurface. The geometry of the resistive feature at the center of these images was compared with the known dimensions and shape of the mineshaft.

Site description

The test site, known as Site B (Fig. 1a), was located in an agricultural area on the location of the former Pewfall Colliery in the north-west of England. The site is cut by the north-west trending Bullstake Fault, with the bedrock material to the south of the fault consisting of undifferentiated sedimentary units of the Middle Coal Measures Formation. To the north of the fault, the site is underlain by Ravenhead Rock sandstone. The bedrock has a general dip of 5^{o} to the south-east and is overlain by a glacial till of approximately 3 m thickness. The north-eastern half of the site is covered by the remnants of a former spoil heap that was also found to be ~3 m thick during site excavations. The topography of the site had previously been measured, with the elevation data recorded at 4 m intervals. A gravel track had been laid to allow access to the site and this encroached onto its south-western corner.

Site B contained a mineshaft of diameter 2.5 m and depth of at least 32 m, which was the approximate depth of the water table. As the shaft was open, it was expected that it would be air-filled above the water table. The site had been leveled and the mine opening re-capped with wood supported on concrete collars (Fig. 1b) and buried again. The location of the mineshaft had subsequently been found using surface geophysical surveys (Wilkinson *et al*., 2005). Boreholes were drilled, to depths of approximately 20 m, with equidistant spacing on the circumference of a 15 m diameter circle centered on the mineshaft. The boreholes were cement lined, so that seismic measurements could also be made, and filled with water to ensure electrical contact with the formation. The elevation range across the survey circle was 0.9 m.

Data acquisition and array optimization

Apparent resistivity measurements were made using the eight different panels shown in Fig. 2. Each borehole contained up to 20 electrodes at 1 m depth spacings. Depending on the borehole separation, a line of either 12 or 16 electrodes connected the boreholes on the surface. These electrodes were in galvanic contact with the ground. The resistivity data were collected using an AGI SuperSting R8 IP system. This is a 200W eight-channel instrument that permits the automated acquisition and storage of up to eight simultaneous potential difference measurements for a given pair of current electrodes.

The question of which types of cross-hole electrical measurements should be made to obtain optimum subsurface resistivity information is still open and a topic of

current research (Goes and Meekes, 2004; Chambers *et al*., 2003; Kuras *et al*., 2003; Bing and Greenhalgh, 2000; Spitzer, 1998). Historically pole-pole measurements have been favored (Poirmeur and Vasseur, 1988) since only relatively few measurements are required to obtain the maximum amount of information. But in this study pole-pole measurements were not used because of their high susceptibility to noise (Beard and Tripp, 1995) and the difficulty of locating remote electrodes on the restricted site. Following the recommendations of Bing and Greenhalgh (2000), four-electrode configurations were used with one current and one potential electrode in each hole (see Figs. 3a and 3b). Configurations with both current and/or both potential electrodes in the same hole were disregarded, since they would have been unduly influenced by current channeling in the conductive borehole water. The channeling effect also causes systematic errors in cross-hole measurements, as the current injection into the formation can no longer strictly be assumed to be point-like. However, Osiensky *et al*. (2004) showed that these errors are only significant within a distance of a few borehole diameters from the borehole. Since the boreholes in this trial had a diameter of 0.1 m, the errors caused by assuming point injection will be small. Each panel also included electrodes on the surface, along a line linking the boreholes. These were used to make surface-to-borehole measurements with one current and one potential electrode on the surface and the others in a borehole (Fig. 3c). Finally standard dipole-dipole measurements were included using the surface electrodes only (Fig. 3d).

To demonstrate the effectiveness of the field measurement scheme, an individual panel is examined in detail. For panel A, 4,702 measurements were made with 11% of type a), 50% of type b), 37% of type c) and 2% of type d). This scheme was chosen to provide image resolution that was as well balanced as possible across the panel, whilst making efficient use of the eight simultaneous measurement channels of the instrument. It is compared to another scheme obtained using an array optimization method based on the model resolution matrix. This method is a faster and more effective version of that proposed by Stummer *et al*. (2004) to determine an optimal scheme for a given number of measurements. Briefly, the model resolution matrix, $\underline{\underline{\mathbf{R}}}$, is defined as

$$\mathbf{m}^{\text{est}} = \underline{\underline{\mathbf{R}}}\mathbf{m}^{\text{true}} \tag{1}$$

(Menke, 1984), where $\mathbf{m}^{\text{est}}$ is the estimate of the model cell resistivities (i.e. the inverted image) and $\mathbf{m}^{\text{true}}$ comprises the true model cell resistivities. It should be emphasized that $\mathbf{m}^{\text{true}}$ is unknown. Therefore an approximation to $\underline{\underline{\mathbf{R}}}$ is used, which is calculated on the basis of a homogeneous half-space (Stummer *et al.,* 2004). This is given by

$$\underline{\underline{\mathbf{R}}} = \left(\underline{\underline{\mathbf{G}}}^{\mathrm{T}}\underline{\underline{\mathbf{G}}} + \underline{\underline{\mathbf{C}}}\right)^{-1}\underline{\underline{\mathbf{G}}}^{\mathrm{T}}\underline{\underline{\mathbf{G}}}, \tag{2}$$

where the matrix element G_{ij} is the sensitivity of the *i*th measurement configuration to a small change in the resistivity of the *j*th model cell, and $\underline{\underline{\mathbf{C}}}$ is the constraint matrix that regularizes the inversion process. The model resolution, *R*, is defined as the leading diagonal of $\underline{\underline{\mathbf{R}}}$. It lies in the range $0 \leq R \leq 1$ and provides a simple measure of how well each model resistivity cell is resolved by the data (0 being unresolved and 1 perfectly

resolved). The optimization procedure begins with a small base set of configurations (in this case, a sparse dipole-dipole array involving only the surface electrodes). Two resolution matrices are calculated, $\underline{\underline{\mathbf{R}}}^{\text{base}}$ for the base set and $\underline{\underline{\mathbf{R}}}^{\text{comp}}$ for the comprehensive set containing all possible four-electrode configurations. Each of the *i* configurations that are *not* included in base set are ranked by a goodness function defined by

$$F_i = \sum_{j=1}^{m} \frac{{G_{ij}}^2}{({G_j}^{\text{sum}})^2} \left(1 - \frac{{R_{jj}}^{\text{base}}}{{R_{jj}}^{\text{comp}}} \right), \tag{3}$$

where *m* is the number of model cells and

$${G_j}^{\text{sum}} = \frac{1}{n_{\text{b}}} \sum_{k=1}^{n_{\text{b}}} \left| G_{kj} \right|, \tag{4}$$

where the index *k* labels all the n_{b} configurations that *are* included in the base set. This goodness function has certain advantages over the one employed by Stummer *et al*. (2004). In their algorithm, Eq. (4) sums over all configurations in the comprehensive set to provide a normalization factor in Eq. (3). Here, only the base configurations are used. This tends to give high weighting to configurations that are linearly independent from the base set. The term in brackets in Eq. (3) selects configurations that improve poorly resolved regions of the model (as in the original algorithm) whilst the modification of Eq. (4) helps ensure that the selected configurations *simultaneously* have good linear independence from the base set. This removes the second, time-consuming, stage of the original procedure involving the separate calculation of the linear independence of each additional configuration. When *F* has been calculated for all the additional

configurations, a small number ($0.15n_b$) of the highest-ranking configurations are added to the base set and the procedure is iterated until the base set contains the desired number of configurations. The number $0.15n_b$ controls a trade-off between speed and performance and was chosen empirically.

To find an optimized scheme to compare with the field measurement scheme, the comprehensive set was constructed from all dipole-dipole configurations (where the electrode order is C1, C2, P1, P2) and all nested configurations (C1, P1, P2, C2). Cross configurations (C1, P1, C2, P2) were not included since they produce very similar results to the nested configurations (Bing and Greenhalgh, 2000). Any configurations with C1 and C2 or P1 and P2 in the same hole were discarded (due to the conductive water-filled boreholes). In addition, any configurations with geometrical factors >2,000 m were discarded to reduce the susceptibility to noise. By considering reciprocity, 3,820 of the configurations used in the field measurement scheme can be shown to be unique. Of these, 3,801 met the above restrictions. This final set of field measurement configurations contained 7% of type a), 49% of type b), 41% of type c) and 3% of type d). For comparison an optimized scheme was constructed, also using 3,801 measurements. Figure 4 shows the model resolution profiles for a) the comprehensive set, b) the optimized scheme and c) the field measurement scheme. Even though the optimized scheme contains only 1.2% of the measurements of the comprehensive set, its model resolution compares very favorably; the ratio of its summed resolution ($S = \sum_{j=1}^{m} R_{jj}$) to

that of the comprehensive set is S_{opt}/S_{comp} = 0.809. More importantly, the field measurement scheme is very close to optimal (S_{field}/S_{comp} = 0.792). It is worth noting that, although the optimized scheme could be used with a multi-channel resistivity instrument, it would be time-consuming. This is because the optimization algorithm gives no consideration to whether or not the chosen configuration has the same pair of current electrodes as any of the previously included configurations. Therefore it is not trivial to combine the optimized configurations into efficient multi-channel measurements.

Each of the eight panels were measured using similar schemes, producing ~33,000 measured apparent resistivity values. About 3% of the measurements had anomalously low apparent resistivity values, which were found to be due to a wiring fault with the equipment. These measurements were removed from the data set before it was processed. Some of the boreholes were less than 20 m deep due to the bentonite plugs that were used to form watertight seals at their bases. Any electrodes that would have extended below the bases of these holes were not used. In addition, all measurements involving the electrode at 1 m depth in borehole 4 were removed since it was occasionally uncovered by drainage. Two of the boreholes required topping up with water during the measurements, but only by a few tens of liters over the period of a day. This small amount would have had a negligible effect on the resistivity of the surrounding formation. Also, any self-potential noise caused by this slow drainage would be small, and in any case would be backed-off automatically by the measurement hardware.

Subsurface resistivity tomograms were obtained by inverting the data using the commercial packages Res2DInv and Res3DInv (Loke and Barker, 1996). Data from individual panels were inverted with Res2DInv, which employs a 2.5D resistivity model, using a smoothness-constrained regularized least-squares optimization technique (Ellis and Oldenburg, 1994; Loke and Barker, 1996; Loke and Lane, 2002) on a 0.5 × 0.5 m grid. For multiple panels, the same technique was used in Res3DInv with 1.0 × 1.0 × 1.0 m cells to produce a 3D resistivity tomogram. The damping factors for these algorithms were refined to produce the best possible images of the shaft given the heterogeneity of the subsurface. In all cases, a homogeneous half-space was used as the initial model, and no upper or lower bounds were set on the model resistivities. The topography was neglected since the surface gradients were shallower than 10° from the horizontal (Tsourlos *et al.*, 1999). In the following section, results are analyzed for cross-hole measurements only (i.e. types a and b), and for the full data sets including hole-surface and surface-surface measurements.

Results and discussion

Three inverted models are presented to demonstrate the effects of data density and coverage on the ability to detect and image the shaft. These involve panel A (a 2.5D inversion), panels A-D and panels A-H (3D inversions) for both field and synthetic data. Generally the quality of the tomographic image should improve as more independent measurements are added by including more panels. However, when moving from a 2.5D

to 3D model, the number of model parameters also increases. Therefore it is possible that 3D models with few panels might be less well constrained than a 2.5D model with a single panel, and hence produce a poorer image.

For the field data, all the images tend to exhibit slightly lower formation resistivities in both the top and bottom few meters of the model. This finding is consistent with borehole conductivity logs, which show a similar trend. The regions of slightly lower resistivity also coincide with increased natural gamma intensities, potentially indicating increased clay content in the surficial materials and in the formation at the base of the boreholes. There is no evidence of the Bullstake fault in the inverted models. This could be because the undifferentiated material and Ravenhead rock might have similar resistivities. It might also be due to uncertainty in the location of the fault, which is an inferred position that could be inaccurate by tens of meters. Therefore the fault may not actually cross the region between the boreholes.

The synthetic data were generated for the same configurations used in the field measurements. A 3D boundary element method, which models the charge accumulation at resistivity boundaries (Li and Oldenburg, 1991), was used to avoid employing the same algorithm for the forward and inverse problems (the so-called “inverse crime”). The synthetic model comprised a vertical cylindrical shaft of 2.5 m diameter, centered on (x = 7.5 m, y = 7.5 m). The shaft began at a depth of 3.0 m, was infinitely resistive, and was embedded in an otherwise homogeneous half-space of 50 Ωm resistivity.

Figure 5 shows the results of 2.5D inversions of synthetic and field data for panel A (indicated by the circular inset). The left-hand diagrams (5a and 5c) show inversions of cross-hole measurements only, whilst those on the right (5b and 5d) use all of the data, including hole-surface and surface-surface measurements. The effects of including surface measurements on the image are similar in the 2.5D and 3D models and are discussed later. Whilst the theoretical models both reveal vertically elongated resistive regions (black) between the boreholes, the shapes of these regions are clearly different to the shape of the shaft. This is probably due to the use of a 3D forward model with a 2.5D inversion. Similarly, the images obtained from the field data exhibit regions of high resistivity in the center of the panel, but also near the boreholes (x = 0 m and x = 15 m). These features are fairly well separated by vertical regions of lower resistivity (white and light gray). The resistive regions in the center of the panels are probably caused by the air-filled mineshaft, but once again the single panel 2.5D inversion has failed to recover the shaft geometry.

The images produced by 3D inversion of measurements from panels A-D are shown for synthetic data in Figs. 6a and 6b, and for field data in Figs 6c and 6d. The synthetic models clearly show a moderately resistive cylindrical region coincident with the location of the mineshaft (highlighted by the dashed cylinders in Figs 6c and 6d). By contrast, the models arising from the field data show strong resistive features around all eight boreholes, but there is no indication of the mineshaft in the center of Fig. 6c, and only a small central resistive feature with limited vertical extent (a “halo”) at a depth of

2.5 m in Fig. 6d. The differences between the synthetic and field models are probably due to the boreholes' cement casings, which are resistive compared to the formation. There are large volumes of the 3D model that do not lie close to any of the four panels, and which are therefore poorly resolved by the data. This means that the data can be fitted sufficiently well by a model that over-estimates the resistive regions near the boreholes, consequently obscuring the contributions of the resistive shaft in the center.

To address this problem, four more panels are added to the data set. Figure 7 shows the results of 3D inversions for synthetic and field data from all eight panels A-H. The additional panels have a clear benefit on the recovered images. In the synthetic images, the size of the cylindrical resistive feature is a slightly better match to the model shaft (shown by the dashed cylinder), and the resistivity contrast is higher than that obtained for panels A-D. The improvements in the images from the field data are more pronounced. There is a resistive structure in the center of each image that is clearly delineated, cylindrical and isolated from the resistive features surrounding the boreholes. Sensitivity calculations show that the measurements made on panels that intersect the mineshaft (A-D) are influenced by its presence by two to three orders of magnitude more than measurements on the outlying panels (E-H). This difference means that, by including data from panels that do not intersect the mineshaft, a model with high resistivity concentrated solely around the boreholes would result in a poor fit. Therefore the inversion algorithm is constrained to produce an image where the presence of the air-filled mineshaft is accurately modeled by a resistive region in the center of the image.

A common feature for all the panel combinations is that the resistivity contrast between the mineshaft and the background is not as high as might be expected for an infinitely resistive air-filled void. This is because the constraints used by the inversion algorithms (Loke and Lane, 2002) tend to reduce resistivity contrasts. It should also be noted that the effects of a resistive target on ERT measurements are not proportional to the resistivity contrast ρ_t / ρ_b, but to the reflection coefficient $\kappa = (\rho_t - \rho_b) / (\rho_t + \rho_b)$, where ρ_t and ρ_b are the resistivities of the target and the background respectively (Li and Oldenburg, 1991). For the synthetic data, $\kappa \sim 0.3$ for the single-panel inversion, $\kappa \sim 0.6$ for the four-panel inversion and $\kappa \sim 0.7$ for the eight-panel inversion. In these terms, apart from the single panel inversion, the discrepancy from the actual value of $\kappa = 1.0$ is not so large. Interestingly, the inversion of the field data for all eight panels yields a higher reflection coefficient of $\kappa \sim 0.9$. Once again this is likely to be an artifact of the resistive borehole casings, which increased all the measured apparent resistivities.

On the test site, measurements were made involving electrodes on the surface as well as in the boreholes. But in an urban environment, it is likely that lines of surface electrodes would be difficult to install. Therefore, another aim of this trial was to compare the images obtained solely from cross-hole measurements with those from cross-hole, hole-surface and surface-surface measurements. A comparison of Figs.5a and 5b shows that adding surface configurations removes the resistive features in the upper two meters of the synthetic 2.5D model, but otherwise does not improve the image. In the synthetic 3D models (Figs. 6 and 7), the geometry and resistivity of the inverted

mineshaft images are somewhat improved by using surface electrodes, especially in the upper half of the model. However, the inclusion of the extra data has also caused an unrealistic conductive annulus to appear around the cylinder of the shaft (this appears as white annular regions in Figs. 6b and 7b). In the field models, the addition of surface configurations has actually degraded the fit to the data, indicated by an increase in the RMS data error from ~2% to ~4% in each case. It has also caused a resistive halo to appear in the center of each model at a depth of 1-2 m. A comparison of Figs. 7c and 7d shows that the surface configurations also distort the image of the shaft. In Fig. 7c, the shaft image is vertical, but in Fig. 7d it leans over towards $x = 0$ between depths of 4 m and 8 m. The exact cause of this effect is unclear, but it does not seem to represent the known structure and geometry of the shaft, which is indicated by the dashed cylinders in Figs. 7c and 7d. The overall effect of adding measurements involving surface electrodes seems to be to distort and possibly over-emphasize surface features. It may be possible to reduce these adverse effects by reducing the weight of the surface configurations in the inversion (Tsourlos *et al*., 2004), but it is not clear that there would be much, if any, improvement compared to the cross-hole only images.

The focus of this paper has been a proof-of-principle study, using eight boreholes symmetrically located about the position of a known mineshaft. Clearly in a more realistic situation the shaft location might not be known, or it might not be possible to place the boreholes in a symmetrical arrangement. Furthermore, for cost reasons, it would be desirable to minimize the number of boreholes required to detect and image the shaft.

We are currently undertaking further research into the effects that these restrictions would have on the quality of the tomographic images.

Conclusions

Cross-borehole ERT measurements were made to detect and image a concealed air-filled mineshaft. In contrast to a previous study, which found that only conductive water-filled cavities could be detected due to advantageous current focusing, it has been shown that the detection of resistive air-filled cavities is possible given a judicious choice of array configurations and panel combinations. The use of a single panel, comprising a set of optimal array configurations, with a 2.5D inversion was only partially successful. It indicated a resistive region in the vicinity of the mineshaft, but failed to recover its geometry. But it was found that greatly improved images could be obtained by using multiple panels and a 3D inversion algorithm. A balanced distribution of panels across the survey area was shown to produce a superior image compared to a concentration of panels that intersected the shaft. The inclusion of outlying panels was required to constrain the corresponding sections of the model. In particular, this enabled the inversion to distinguish the contributions to the higher apparent resistivity data that were caused by the mineshaft from those caused by the resistive cement linings of the boreholes.

In general, it appears that careful consideration should be given to the number and arrangement of panels to ensure even coverage of a survey area when imaging void

spaces using 3D cross-borehole ERT. For each individual panel, an optimized set of electrode configurations should be used to maximize the amount of information collected from the measurements. It was shown that the inclusion of configurations involving on-panel surface electrodes did not generally improve the images. However, if the number of required boreholes is prohibitive in terms of time or cost, it might be advantageous to include *off*-panel surface electrodes to increase the coverage of regions that would otherwise be poorly constrained. Provided that these points are taken into account, the results indicate that cross-borehole ERT can produce good quality images of air-filled cavities, and merits serious consideration as an alternative, or complementary, technique to cross-borehole seismic tomography.

Acknowledgements

This work was funded by the Coal Authority. The authors gratefully appreciate the advice given by Prof. P. Styles throughout this project. We also thank Dr. P. I. Tsourlos for his helpful comments. This paper is published with permission of the Chief Executive of the Coal Authority and the Executive Director of the British Geological Survey (NERC).

References

Beard, L.P., and Tripp, A.C., 1995, Investigating the resolution of IP arrays using inverse theory: Geophysics, **60**, 1326-1341.

Bing, Z., and Greenhalgh, S.A., 2000, Cross-hole resistivity tomography using different electrode configurations: Geophysical Prospecting, **48**, 887-912.

Chambers, J.E., Kuras, O., Meldrum, P.I., and Ogilvy, R.D., 2003, Comparison of fundamental modes of illumination for cross-hole electrical impedance tomography: Part I - sensitivity analysis: Proceedings of the 9th meeting of the EEGS, Prague, Czech Republic.

Ellis, R.G., and Oldenburg, D.W., 1994, Applied Geophysical Inversion: Geophysical Journal International, **116**, 5-11.

Goes, B.J.M., and Meekes, J.A.C., 2004, An effective electrode configuration for the detection of DNAPLs with electrical resistivity tomography: Journal of Environmental and Engineering Geophysics, **9**, 127-141.

Kuras, O., Chambers, J.E., Meldrum, P.I., and Ogilvy, R.D., 2003, Comparison of fundamental modes of illumination for cross-hole electrical impedance tomography: Part II - synthetic modelling. Proceedings of the 9th meeting of the EEGS, Prague, Czech Republic.

Li, Y., and Oldenburg, D.W, 1991, Aspects of charge accumulation in d.c. resistivity experiments: Geophysical Prospecting, **39**, 803-826.

Loke, M.H., and Barker, R.D., 1996, Practical techniques for 3D resistivity surveys and data inversion: Geophysical Prospecting, **44**, 499-523.

Loke, M.H., and Lane, J.W., 2002, The use of constraints in 2D and 3D resistivity modelling: Proceedings of the 8th meeting of the EEGS, Aveiro, Portugal.

Maillol, J.M., Seguin, M.K., Gupta, O.P., Akhauri, H.M., and Sen, N., 1999, Electrical resistivity tomography survey for delineating uncharted mine galleries in West Bengal, India: Geophysical Prospecting, **47**, 103-116.

Menke, W., 1984, Geophysical data analysis: Discrete Inverse Theory: Academic Press, Orlando.

Misiek, R., Gebhardt, F., Orlowsky, D., and Lehmann, B., 2001, Tomographic investigations for the detection of cavities below buildings: Proceedings of the 7th meeting of the EEGS, Birmingham, UK.

Nath, S.K., 2004, Cross-hole seismic tomography – A geophysical tool for detecting mine galleries: National Academy Science Letters – India, **27**, 77-94.

Orlowsky, D., Hunfield, U., and Lehmann, B., 2003, Seismic tomography to explore cleft zones below houses in the area of a stress system induced by deep coal mining activities. Proceedings of the 9th meeting of the EEGS, Prague, Czech Republic.

Osiensky, J.L., Nimmer, L., and Binley, A.M., 2004, Borehole cylindrical noise during hole-surface and hole-hole resistivity measurements: Journal of Hydrology, **289**, 78-94.

Poirmeur, C., and Vasseur, G., 1988, Three-dimensional modeling of a hole-to-hole electrical method: Application to the interpretation of a field survey: Geophysics, **53**, 402-414.

Rechtien, R.D., Greenfield, R.J., and Ballard Jr., R.F., 1995, Tunnel signature prediction for a cross-borehole seismic survey: Geophysics, **60**, 76-86.

Spitzer, K., 1998, The three-dimensional DC sensitivity for surface and subsurface sources: Geophysical Journal International, **134**, 736-746.

Stummer, P., Maurer, H., and Green, A.G., 2004, Experimental design: Electrical resistivity data sets that provide optimum subsurface information: Geophysics, **69**, 120-139.

Tsourlos, P.I., Syzmanski, J.E., and Tsokas, G.N., 1999, The effect of terrain topography on commonly used resistivity arrays: Geophysics, **64**, 1357-1363.

Tsourlos, P.I., Ogilvy, R.D, and Papazachos, C., 2004, Borehole-to-surface ERT inversion: Proceedings of the 10th meeting of the EEGS, Utrecht, The Netherlands.

Wilkinson, P.B., Chambers, J.E., Meldrum, P.I., Ogilvy, R.D., Mellor, C.J., and Caunt, S., 2005, A comparison of self-potential tomography with electrical resistivity tomography for the detection of abandoned mineshafts: Journal of Environmental and Engineering Geophysics, **10**, 381–389.

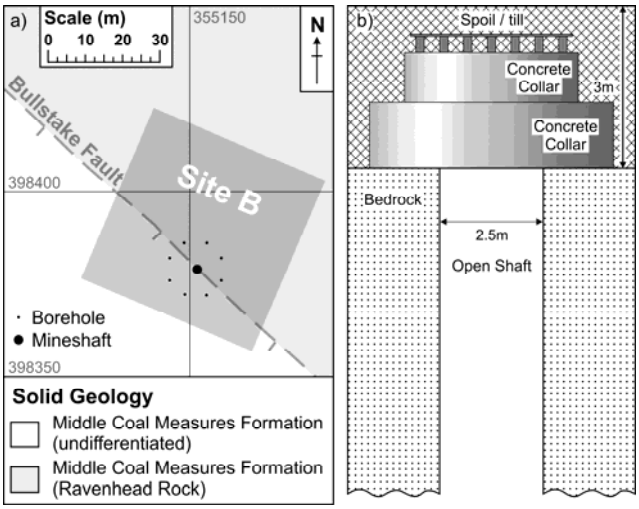

Figure 1. a) Plan of site B showing scale, orientation, solid geology, boreholes and mineshaft locations. b) Schematic diagram of shaft showing concrete collars, wooden capping (in dark gray) and spoil thickness.

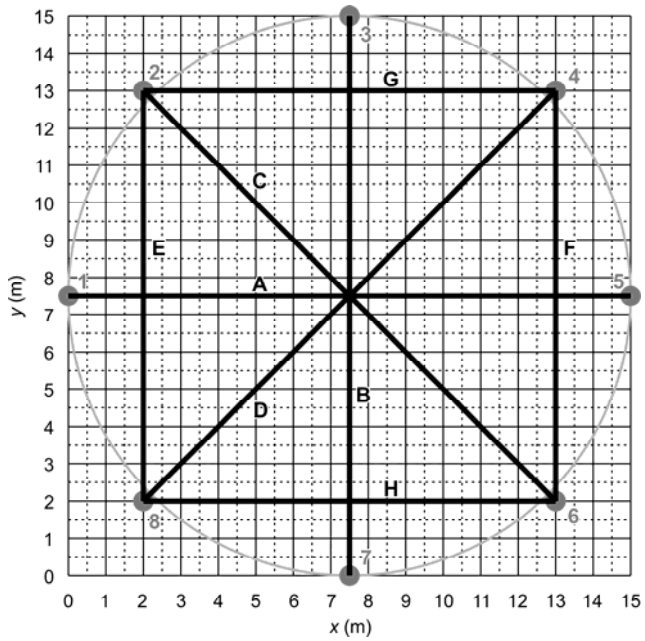

Figure 2. Locations of boreholes (filled circles, labeled 1-8) and measurement panels (bold lines, labeled A-H).

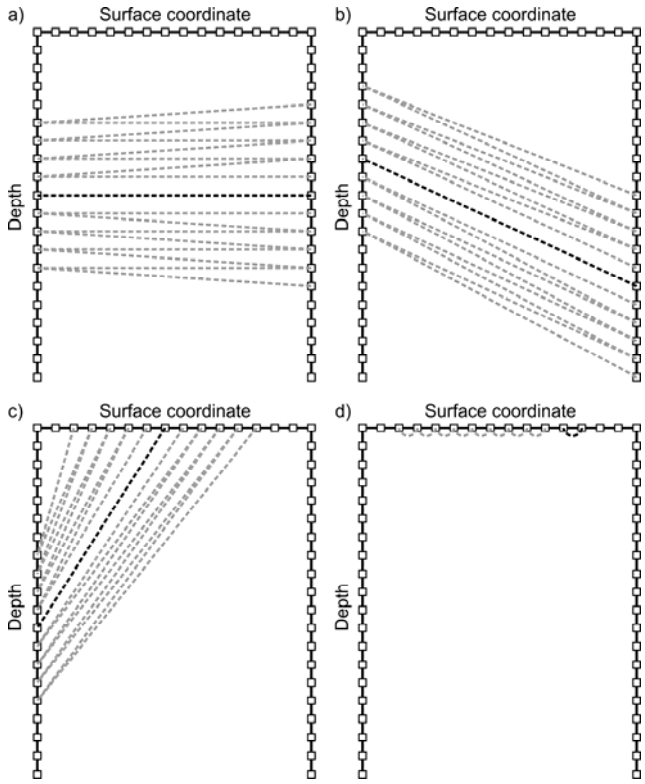

Figure 3. Schematic diagrams showing measurement types. a) Horizontal cross-hole, b) diagonal cross-hole, c) hole-surface and d) surface-surface. Open boxes indicate electrodes, black dashed lines show current electrode pairs and gray dashed lines show typical groups of multiple potential electrode pairs.

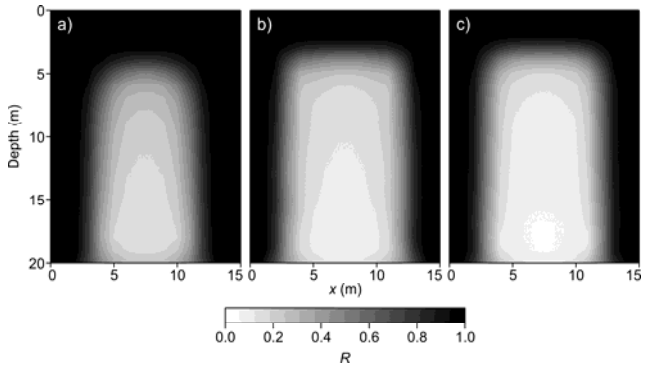

Figure 4. Model resolution *R* for single panel measurements sets comprising a) all 316,640 configurations, b) 3,801 optimized configurations and c) 3,801 configurations used in field measurements.

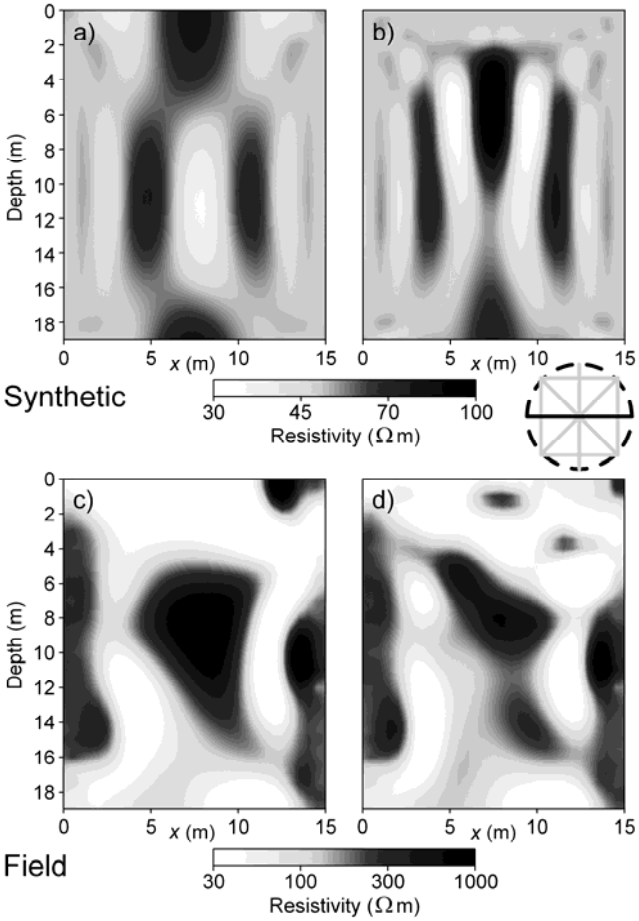

Figure 5. 2D resistivity tomograms for panel A for synthetic data a) without surface configurations and b) with surface configurations and for field data c) without surface configurations and d) with surface configurations. Circular inset indicates active panel (black line).

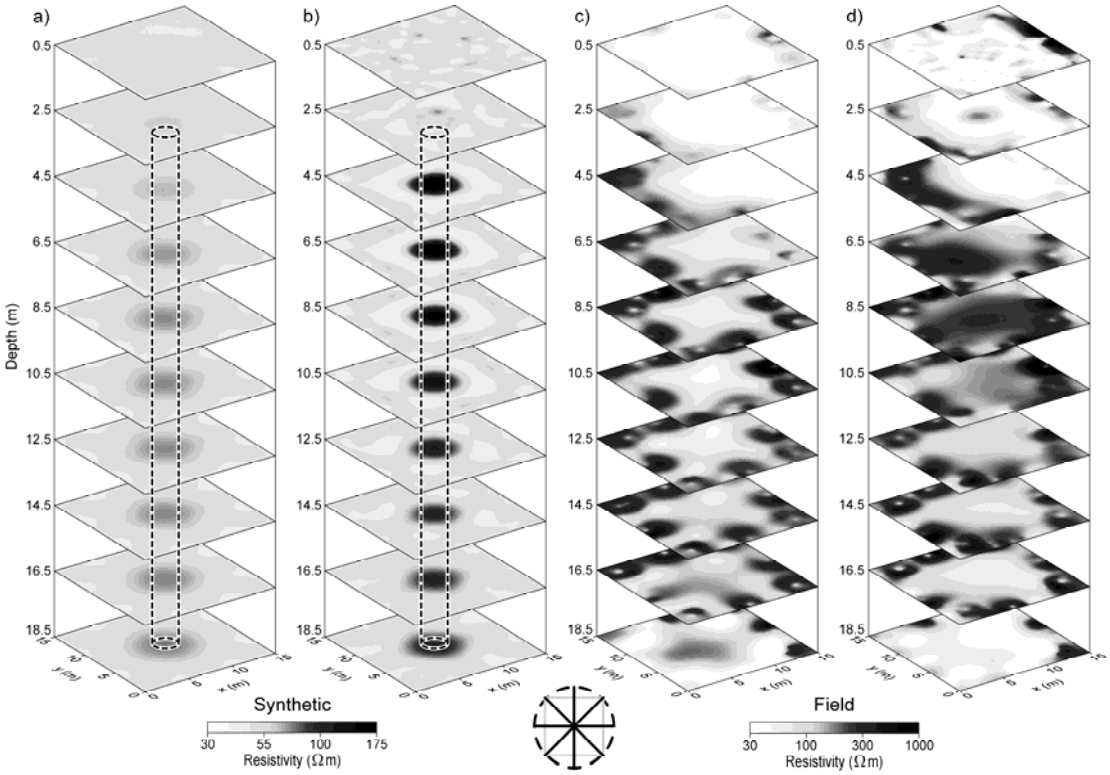

Figure 6. 3D resistivity tomograms for panels A-D for synthetic data a) without surface configurations and b) with surface configurations and for field data c) without surface configurations and d) with surface configurations. Dashed cylinders show location and extent of synthetic mineshaft. Circular inset indicates active panels (black lines).

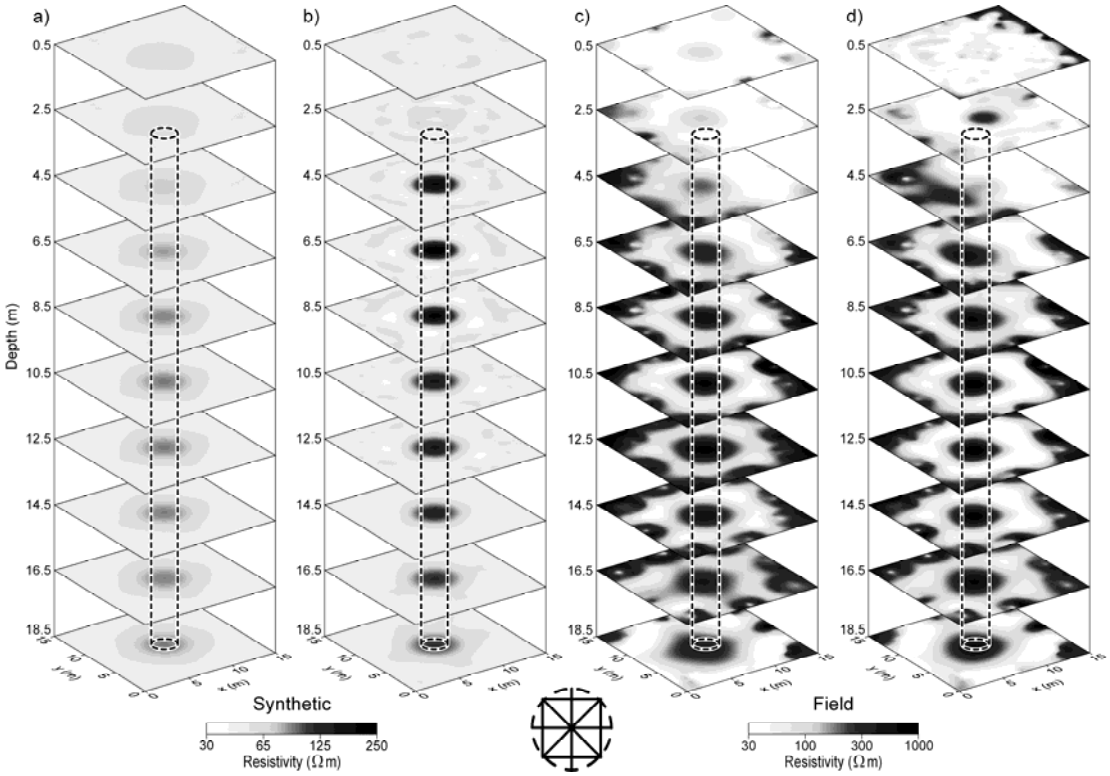

Figure 7. 3D resistivity tomograms for panels A-H for synthetic data a) without surface configurations and b) with surface configurations and for field data c) without surface configurations and d) with surface configurations. Dashed cylinders show location and extent of mineshaft. Circular inset indicates active panels (black lines).